Supplementary Information

Molecular-scale insights into the electrical double layer at oxide-electrolyte interfaces

Chunyi Zhang[1], Marcos Calegari Andrade[2], Zachary K. Goldsmith [1], Abhinav S. Raman[1], Yifan Li[1], Pablo M. Piaggi[1,3,4], Xifan Wu[5], Roberto Car[1]*, and Annabella Selloni[1]*

[1] *Department of Chemistry, Princeton University, Princeton, New Jersey 08544, USA*

[2] *Materials Science Division, Lawrence Livermore National Laboratory, Livermore, California 94550, USA*

[3] *CIC nanoGUNE BRTA, Tolosa Hiribidea 76, Donostia / San Sebastián 20018, Spain*

[4] *Ikerbasque, Basque Foundation for Science, Bilbao 48013, Spain*

[5]*Department of Physics, Temple University, Philadelphia, Pennsylvania 19122, USA*

Email: rcar@princeton.edu, aselloni@princeton.edu

Table of Contents

1. Details of the training dataset

Supplementary Table 1. Details of the training dataset: systems, constituents, and number of configurations (N) for each system.

Systems	**Constituents**	***N***
1. One water molecule in a vacuum	1 H_2O	127
2. Bulk water	64 H_2O	2,870
3. Bulk $NaCl_{(aq)}$	64 H_2O + 1~6 NaCl	5,710
4. Bulk $NaOH_{(aq)}$	40~63 H_2O + 1~12 NaOH	4,466
5. Bulk $HCl_{(aq)}$	44~64 H_2O + 1~12 HCl	3,244
6. Bulk TiO_2	36 TiO_2	1,119
7. Gas-phase water on anatase (101)	72 TiO_2 + 1~2 H_2O	192
8. Anatase (101)-liquid water interface	60 TiO_2 + 82 H_2O	3,331
9. Anatase (101)-$NaCl_{(aq)}$ interface	60 TiO_2 + 82 H_2O + 1 NaCl	3,794
10. Anatase (101)-$NaOH_{(aq)}$ interface	60 TiO_2 + 60~81 H_2O + 1~12 NaOH	2,590
11. Anatase (101)-$HCl_{(aq)}$ interface	60 TiO_2 + 71~82 H_2O + 1~12 HCl	1,718
12. Bulk $NaCl_{(aq)}$ +$NaOH_{(aq)}$	61 H_2O + 1 NaCl + 1 NaOH	147
13. Bulk $NaCl_{(aq)}$ +$HCl_{(aq)}$	61 H_2O + 1 NaCl + 1 HCl	152
14. Anatase (101)-$NaCl_{(aq)}$+$NaOH_{(aq)}$ interface	60 TiO_2 + 74~80 H_2O + 1~2 NaCl + 1~4 NaOH	346
15. Anatase (101)-$NaCl_{(aq)}$+ $HCl_{(aq)}$ interface	60 TiO_2 + 78~81 H_2O + 1~2 NaCl + 1~4 HCl	297

2. Validation

2.1 Spread parameter

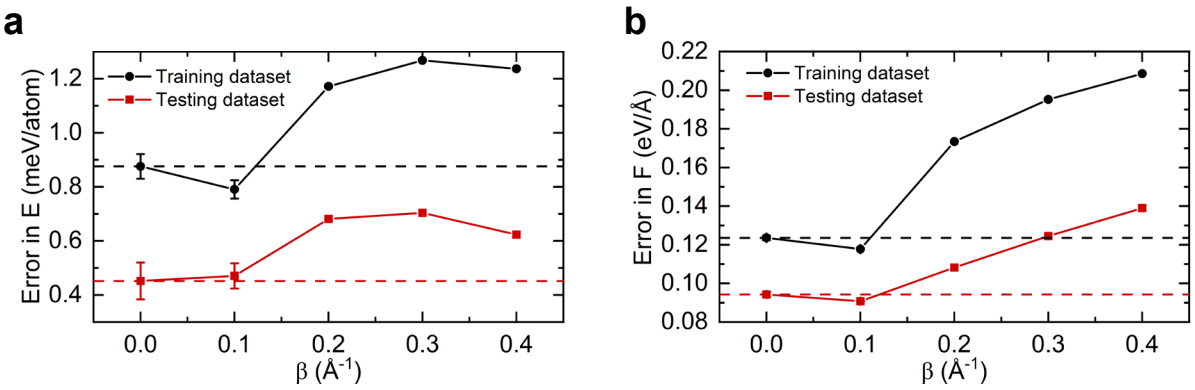

Supplementary Figure 1. Root mean square error of the deep potential long-range (DPLR) predicted **a**, energy, and **b,** atomic force as a function of the spread parameter $\boldsymbol{\beta}$, evaluated on training and testing datasets. The horizontal dashed lines indicate the errors predicted by deep potential short-range (DPSR).

2.2 Time convergence

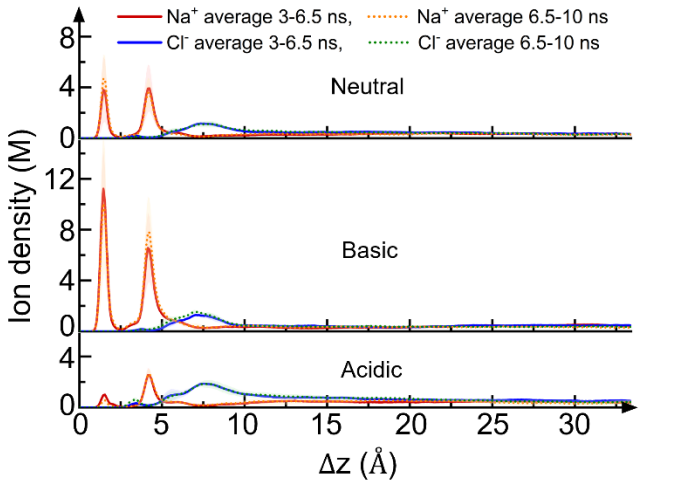

Supplementary Figure 2. Ion density distributions as a function of distance, $\Delta z = z - z_{\text{surface}}$, from the solid surface, obtained from 330 K DPLR simulations of anatase (101) in contact with

different electrolytes. The solid lines represent averages over the period from 3 to 6.5 ns, while the dashed lines represent averages over the period from 6.5 to 10 ns.

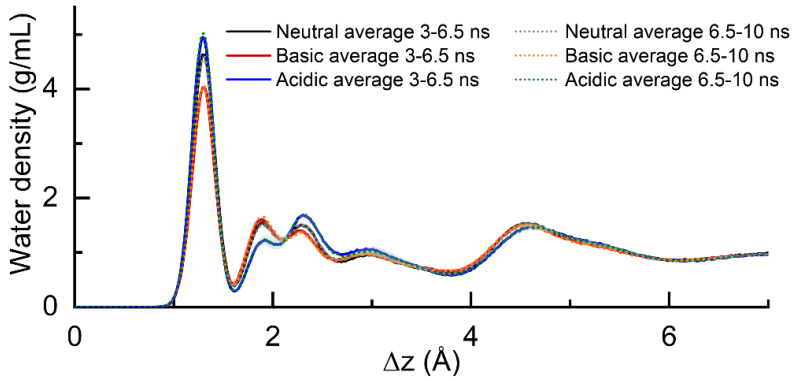

Supplementary Figure 3. Water density distributions as a function of distance, $\Delta z = z - z_{\text{surface}}$, from the solid surface, obtained from 330 K DPLR simulations of anatase (101) in contact with different electrolytes. The solid lines represent averages over the period from 3 to 6.5 ns, while the dashed lines represent averages over the period from 6.5 to 10 ns.

2.3 Energies, atomic forces, and WCs

We assessed the performance of our DPLR and deep Wannier (DW) deep neutral network (DNN) models by comparing their predicted energies, atomic forces, and Wannier centroids (WCs) for the testing dataset to the results of DFT-SCAN calculations. Supplementary Fig. 4 shows that the DNN models reproduce well the DFT results. The root-mean-squared errors of the energies, atomic forces, and WCs predicted by the DNN models with respect to DFT are 0.47 meV/atom, 0.091 eV/Å, and 0.003 Å, respectively. The coefficient of determination, $\boldsymbol{R^2}$, for energy, force, and WC are 0.96, 0.99, and 0.99, respectively, indicating that our DNN models can accurately reproduce the DFT results.

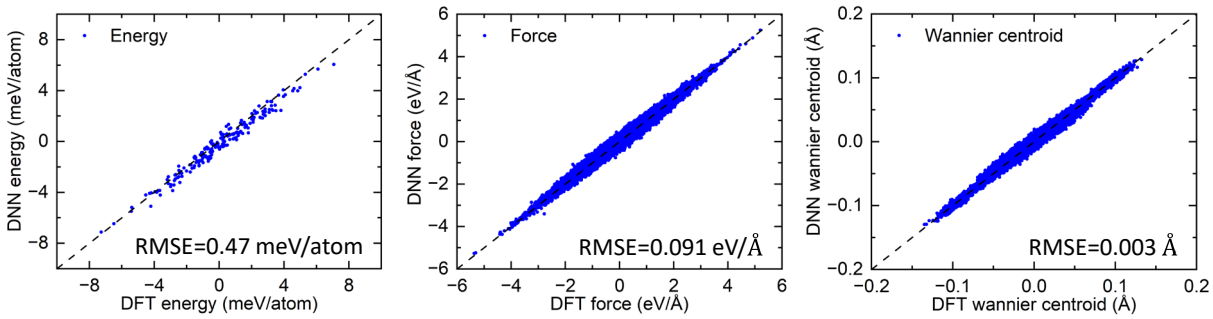

Supplementary Figure 4. Comparison between the energies, atomic forces, and Wannier centroids predicted by the DNN models and DFT-SCAN calculations. The average value of the energy of each system was shifted to zero for better visualization.

To further validate the accuracy of the DNN models for the specific adsorption of Na^+ ions at the TiO_2 surface, we compared energies, forces, and WCs from our DNN models and DFT for configurations with specific adsorption. In detail, we conducted DPLR molecular dynamics simulation of a relatively small model of the TiO_2-$NaOH_{(aq)}$ interface, comprising a five-layer (1×3) anatase (101) slab with 81 H_2O molecules and 1 NaOH ion pair. The simulation was conducted within the canonical ensemble at 330 K for 600 ps, with the Na^+ ion adsorbed at the surface. The initial 100 ps of the simulation was discarded for equilibration purposes. From the subsequent 500 ps, 50 configurations were uniformly extracted from the trajectory. As shown in Supplementary Fig. 5, the *z*-distances of the Na^+ ion from the solid surface of these 50 configurations fluctuate around 1.5 Å, which corresponds to the first Na^+ peak of ion density distribution (see Fig. 2b of the main manuscript), indicating that the Na^+ ion is adsorbed at the TiO_2 surface in these configurations. Supplementary Fig. 5b-d compares the energies, atomic forces, and WCs predicted by our DNN models with the results from DFT-SCAN calculations, for these 50 configurations with specific adsorption. It can be seen that the DNN models accurately reproduce the DFT results, with root-mean-squared errors of 0.38 meV/atom for energies, 0.095 eV/Å for atomic forces, and 0.003 Å for WCs.

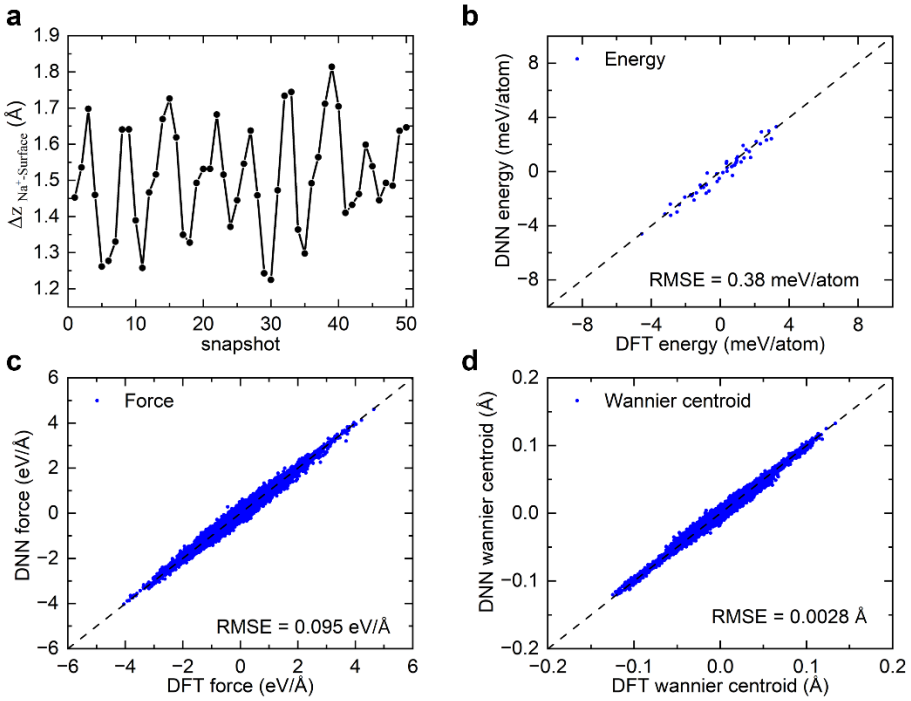

Supplementary Figure 5. a Distance of the Na^+ ion from the solid surface, $\Delta z_{\mathrm{Na+-surface}} = z_{\mathrm{Na+}} - z_{\mathrm{surface}}$, in the *z*-direction for the 50 selected snapshots. The position of the solid surface, z_{surface}, corresponds to the average position of the O_{2c} sites. **b-d,** Comparison between the energies, atomic forces, and Wannier centroids predicted by the DNN models and DFT-SCAN calculations for the 50 configurations in **a**. The average value of the energy was shifted to zero for better visualization.

2.4 Radial distribution functions and water density profiles

We also compared the radial distribution functions of selected atomic type pairs and water density profiles at the anatase (101)-water interface predicted by DPLR molecular dynamics (DPLR MD) with DPSR molecular dynamics (DPSR MD) and previously reported results from *ab initio* molecular dynamics (AIMD)[1]. As shown in Supplementary Fig. 6, the agreement between DPLR-MD, DPSR-MD, and AIMD simulations (both on the time scale of ~ 40 ps) is quite satisfactory.

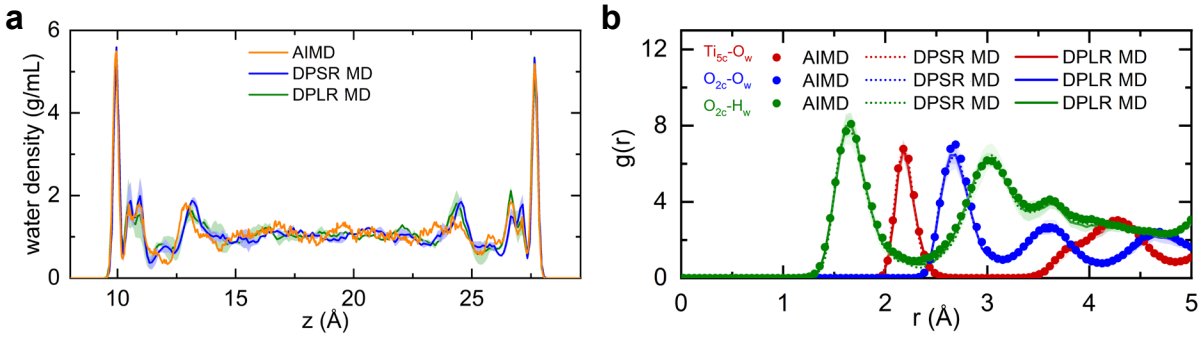

Supplementary Figure 6. Comparison between the predictions of DPLR MD, DPSR MD, and AIMD[1] simulations (both on a time scale of ~ 40 ps) for the water-anatase (101) interface: **a,** Water density profile along the direction perpendicular to the TiO_2 surface; **b,** radial distribution functions, $\boldsymbol{g(r)}$, of selected atomic type pairs. The definition of Ti_{5c} and O_{2c} is given in the main manuscript, and O_w denotes the water oxygen atoms. Shaded areas indicate the standard deviation obtained from two independent DPLR MD or two independent DPSR MD simulations.

2.5 Interfacial water dissociation

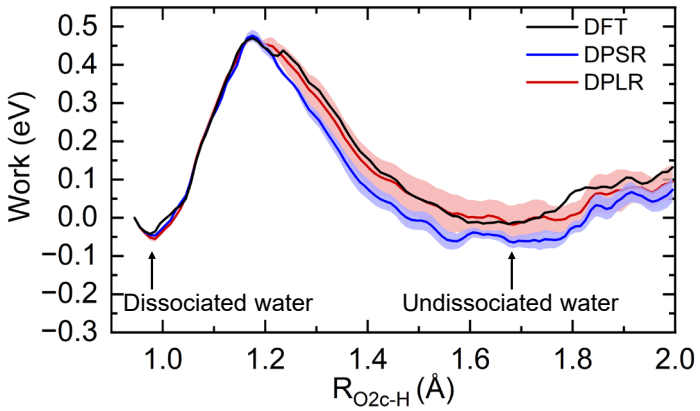

Supplementary Figure 7. Comparison between DFT, DPSR, and DPLR results for the work to move an H^+ from a surface O_{2C} to an OH^- adsorbed on an adjacent Ti_{5c} at the anatase (101)-water interface. The two local minima correspond to dissociated and undissociated water. Shaded areas indicate the standard deviation obtained from two independent DNN models.

Following Ref. 2, we computed the work required to move an H^+ from a surface O_{2C} to an OH^- adsorbed on an adjacent Ti_{5c} at the anatase (101)-water interface (see below for computational details). Supplementary Fig. 7 shows the results obtained using DFT, DPSR, and DPLR. DPLR

is in closer agreement with DFT than DPSR. The higher energy of undissociated water predicted by DPLR in comparison to DPSR is in accordance with the larger water dissociation fraction observed in DPLR-MD simulations ($14.1 \pm 2.0\%$) relative to that reported by previous DPSR simulations ($5.6 \pm 0.5\%$)[2].

Computational details. To compute the curves in Supplementary Fig. 7, we conducted a 2.5 ns enhanced sampling simulation with only one of our two DPLRs (referred to as DPLR model1), and the TiO_2-water interface was modeled as a (1×3) anatase (101) slab in contact with a 20 Å slab of water. Using a reaction coordinate defined as the minimum distance between a particular surface O_{2C} atom and any H atom in the system (denoted R_{O2c-H}), we applied a static external bias potential $V(R_{O2c-H}) = -18exp\left(-\frac{(R_{O2c-H}-1.17)^2}{0.04}\right) - 2.4exp\left(-\frac{(R_{O2c-H}-1.36)^2}{0.04}\right)$, which was designed to enhance the water dissociation at the interface (see Ref. 19 for further details). We extracted atomic configurations with different R_{O2c-H} values from the simulation trajectory and calculated the force projected on the unit vector connecting an O_{2C} to the nearest H atom of these configurations using two DPLR models ($f_{\mathrm{DPLR\ model}j}$, j=1, 2), as well as two DPSR models ($f_{\mathrm{DPSR\ model}j}$), and DFT ($f_{\mathrm{DFT}}$).

Since the configurational space was explored using DPLR model1, a reweighing process was necessary for the other models. The reweighted force was performed as follows:

$$f_*^{reweighted} = \frac{< f_* \times e^{\frac{E_{\mathrm{DPLR\ model1}} - E_*}{k_B T}} >_{\mathrm{DPLR\ model1}}}{< e^{\frac{(E_{\mathrm{DPLR\ model1}} - E_*)}{k_B T}} >_{\mathrm{DPLR\ model1}}}, \quad (1)$$

where * could be any of the two DPLR models, two DPSR models, or DFT. The notation $< \cdots >_{\mathrm{DPLR\ model1}}$ indicates that the average is conducted on the configurations extracted from the DPLR model1 trajectory, k_B is the Boltzmann constant, T is the simulation temperature which equals to 330 K, and E_* is the energy of the system predicted by model *. The work associated with proton transfer was then computed as the integral of reweighted forces.

We note that the increase in water dissociation fraction from 5.6% in a previous study[2] to 14% in this work is not due to the addition of NaCl, but rather the result of transitioning from DPSR to DPLR simulations. To further clarify this, we conducted DPLR molecular dynamics simulations of the TiO_2-neat water interface, using the same simulation cell size and simulation conditions as the TiO_2-$NaCl_{(aq)}$ interface. As shown in Supplementary Fig. 8, the averaged water

dissociation fraction of the TiO_2-water interface after equilibrium is $13.6 \pm 2.1\%$, which agrees with the water dissociation fraction of $14.1 \pm 2.0\%$ observed at the TiO_2-$NaCl_{(aq)}$ interface.

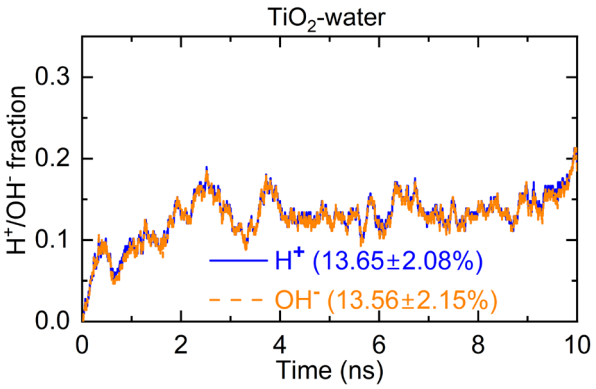

Supplementary Figure 8. Time evolution of the surface H+ and OH- coverage at TiO2-water interface. The legends list the surface ion coverages averaged between 3-10 ns.

2.6 Specific adsorption of Na+ ion

To calculate the potential of mean force for the specific adsorption of Na^+ ion, we conducted ten DPLR molecular dynamics simulations of the TiO_2-$NaOH_{(aq)}$ interface, where we used a five-layer (1×3) anatase (101) slab interfaced with 81 H_2O molecules and 1 NaOH ion pair. Each simulation was conducted within the canonical ensemble at 330 K for 2 ns using our DPLR model1. We extracted 330 atomic configurations with different distances of the Na^+ ion from the solid surface, $\Delta z_{\mathrm{Na+-surface}} = z_{\mathrm{Na+}} - z_{\mathrm{surface}}$. The force along z on the Na^+ ion was calculated using two DPLR models ($f_{\mathrm{DPLR\ model}j}$, j=1, 2) and DFT (f_{DFT}). Since the configurational space was explored using DPLR model1, a reweighting process was performed using Eq. (1). The potential of mean force was then computed as the integral of reweighted forces. As shown in Supplementary Fig. 9, the potential of mean force for the specific adsorption of a Na^+ ion calculated by DPLR agrees well with the DFT result, with both DPLR and DFT results showing a minimum at around 1.5 Å, which is the position of the first Na^+ peak in the ion density distribution (see Fig. 2b of the main manuscript) and corresponds to the adsorbed Na^+ ion. This indicates that our DPLR model can well reproduce the DFT results for the adsorption of Na^+ at the TiO_2 surface.

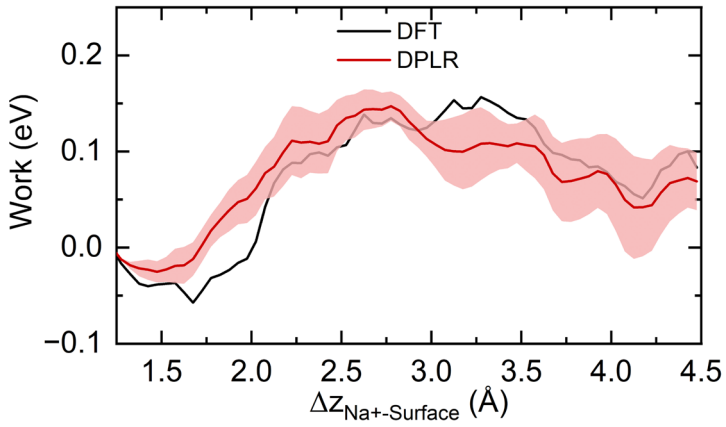

Supplementary Figure 9. Potential of mean force for the specific adsorption of a Na^+ ion. The black and red lines represent the results obtained from DFT and DPLR, respectively. Shaded areas indicate the standard deviation obtained from two independent DPLR models.

3. Comparing the ion distributions from DPSR and DPLR simulations

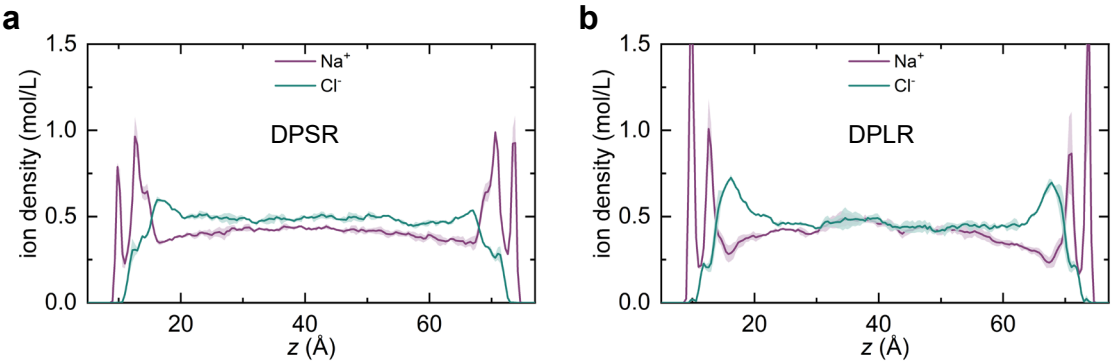

Supplementary Figure 10. Plane-averaged ion distributions along the *z*-direction for the TiO_2-NaCl solution interface obtained from DPSR and DPLR MD simulations. The 5 ns simulations were conducted within the canonical ensemble at 600 K, rather than 330 K, to leverage the faster statistical convergence achievable at elevated temperatures.

Supplementary Fig. 10 shows the ion distributions at 600 K obtained from DPSR and DPLR MD simulations. Due to the screening effect of the EDL, the solution should recover its bulk properties in the central region (away from the interface) and thus have equal densities of Na^+ and Cl^- ions. DPSR simulations predict instead a ~ 0.06 M higher density of Cl^- vs Na^+ ions in the central region (Supplementary Fig. 10a). Because of the lack of long-range electrostatic

interactions, there is no energy penalty for the unphysical charge imbalance in the DPSR models. The inclusion of long-range electrostatic interactions corrects this issue, as shown by the DPLR results in Supplementary Fig. 10b. The ion distributions within the EDL are also changed after including these long-range interactions, confirming that these are essential for the correct description of the EDL.

4. PH point of zero proton charge (pH_{PZC})

As a reference for the surface charging results reported in the main text (Fig. 1), we estimated the pH_{PZC} of the aqueous anatase (101) surface using our DPLR model. The pH_{PZC} of an oxide surface is determined by the acid dissociation constants (pK_as) of the surface acid-base active sites that can accept or release protons. On anatase (101), there are two types of such sites, the O_{2c} and the Ti_{5c} sites, and the pH_{PZC} is simply the average of the pK_as of these sites, i.e., $pH_{PZC} = (pK_{a,O_{2c}} + pK_{a,Ti_{5c}})/2$.

We evaluated these pK_as from the free energy changes associated with the following reactions:

reaction 1 (for the O_{2c} site)

$$O_{2c}H^+ + H_2O_{(aq)} \rightarrow O_{2c} + OH_{3\,(aq)}^+ \quad (2)$$

reaction 2 (for the Ti_{5c} site)

$$Ti_{5c}H_2O + H_2O_{(aq)} \rightarrow Ti_{5c}OH^- + H_3O_{(aq)}^+ \quad (3)$$

This study was performed via DPLR MD and enhanced sampling (well-tempered metadynamics) simulations using the LAMMPS package[3] with the DeepMD-kit[4] and PLUMED[5]. For each reaction, we carried out two independent DPLR simulations, from which we derived the average properties and their error bars. The simulations were performed in the canonical ensemble at 330 K for 2ns on a system comprised of a (1×3) anatase (101) slab (exposing 12 O_{2c} and Ti_{5c} sites) in contact with a 20 Å thick layer of water. For the enhanced sampling, we used the collective variables (CVs) introduced in Ref. [6] and followed the procedure described in Ref. [7]. For reaction 1, the reference state had 11 undissociated water molecules adsorbed at 11 Ti_{5c} sites and one dissociated water molecule with OH^- adsorbed at a Ti_{5c} site and H^+ adsorbed at a nearby O_{2c} site. We applied restraints to only allow proton transfer between the specific O_{2c} site and liquid water. For reaction 2, the reference state had 12 undissociated water molecules adsorbed at 12 Ti_{5c} sites. Here, restraints were introduced to permit only one of the 12 water molecules to exchange one

proton with liquid water at a time. These constraints were essential for the successful implementation of the CVs[6,7].

Supplementary Fig. 11 shows the free energy surface of the two reactions as a function of the s_p and s_d CVs defined in Refs. [6,7]. For each reaction, the deprotonation free energy, ΔF, was calculated as the free energy difference between the deprotonated state ($s_p \approx 1, 10$ Å $< s_d <$ 14 Å) and the protonated state ($s_p \approx 0, s_d \approx 0$). For the deprotonated state, the range 10 Å $< s_d <$ 14 Å ensures that the released proton is sufficiently distanced from both the upper and lower interfaces, preventing interfacial effects on the free proton. In this way, ΔF for reactions 1 and 2 were calculated to be 37.25 ± 0.62 and 51.00 ± 0.65 kJ/mol, respectively. Using $pK_a = \Delta F / 2.303 k_B T$, we obtained $pK_{a,O_{2c}} = 5.9 \pm 0.1$ and $pK_{a,Ti_{5c}} = 8.1 \pm 0.1$, yielding $pH_{PZC} = 7.0 \pm 0.1$. This result compares well to the experimental pH_{PZC} range of 6 ± 1[8-10].

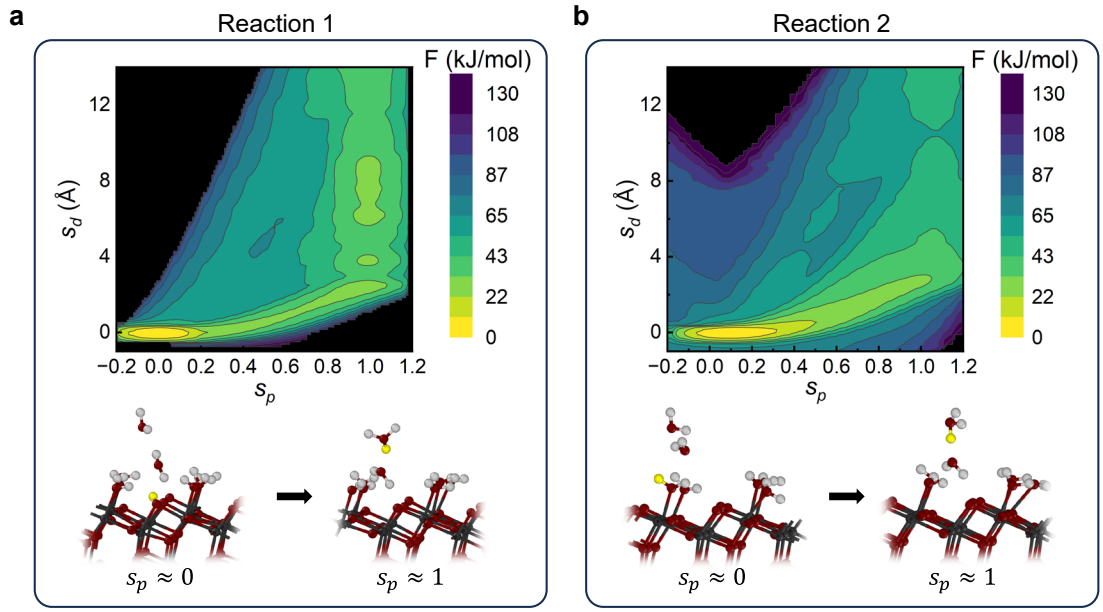

Supplementary Figure 11. Free energy surface for **a,** reaction 1 and **b,** reaction 2. The bottom panels show the representative snapshots of the proton transfer process from $s_p \approx 0$ to $s_p \approx 1$. For visualization purposes, only the relevant atoms are shown. Color code: Ti, grey; O, red; H, white (the proton being transferred is highlighted in yellow).

5. Ion residence time

The probability for an ion to reside within the ionic peak associated with the inner Helmholtz plane (IHP) or one of the intermediate Helmholtz planes (IMHPs) was calculated according to

$$P(\Delta t) = \sum_{t_0=0}^{t_{max}} \frac{\sum_{i=1}^{N} I_i(t_0, t_0 + \Delta t)}{N(t_0)}, \quad (4)$$

where $I_i(t_0, t_0 + \Delta t)$ is the indicator function that equals one only when an ion remains in a specific peak for the entire period between t_0 and $t_0 + \Delta t$. N is the total number of Na^+ or Cl^- ions in the system, and $N(t_0)$ is the number of ions in the specific peak at time t_0. To reduce the effects of instantaneous fluctuations of ions across different peaks, any peak crossing with a time interval less than 1 ps was neglected. The ranges of the ionic peaks are defined by the minima in ion density distributions as functions of distance Δz from the solid surface in Fig. 2b of the main manuscript. The ionic peak associated with IHP consists of Na^+ ions in the range $0\ \text{Å} < \Delta z < 2.55\ \text{Å}$; the peak associated with IMHP1 consists of Cl^- ions in the range $0\ \text{Å} < \Delta z < 4.25\ \text{Å}$; the peak associated with IMHP2 consists of Na^+ ions in the range $2.55\ \text{Å} < \Delta z < 7.35\ \text{Å}$. The ion residence time τ is calculated as $\tau = \int_0^\infty P(t)tdt / \int_0^\infty P(t)dt$.

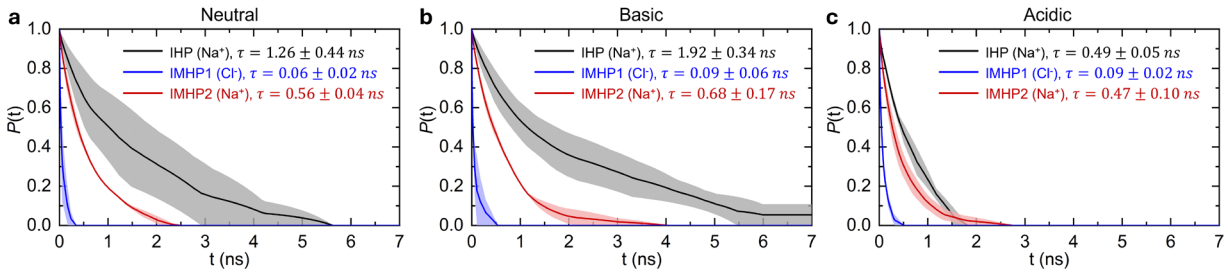

Supplementary Figure 12. Residence probabilities of the Na^+ and Cl^- ions within the inner Helmholtz plane (IHP) and intermediate Helmholtz planes (IMHP1 and IMHP2) for the **a,** neutral, **b,** basic, and **c,** acidic systems. All results and error bars (shaded areas) were derived from simulations using two independent DPLR models. The legends list the ion residence time τ.

As shown in Supplementary Fig. 12, Na^+ ions in the IHP have long residence times on the order of nanoseconds due to strong chemical adsorption at surface O_{2C} sites. In contrast, Na^+ ions

in IMHP2 have shorter residence times on the order of hundreds of picoseconds because their interaction with the solid surface is indirect, mediated by surface water molecules. In both IHP and IMHP2, Na^+ ions exhibit longer residence times in basic systems and shorter residence times in acidic systems. This difference is attributed to the stabilization of cations by negatively charged surfaces in basic conditions and the destabilization of cations by positively charged surfaces in acidic conditions. Finally, Cl^- ions in IMHP1 have much shorter residence times, on the order of tens of picoseconds, because the electronegativity of O_{2C} surface ions repels Cl^- ions from the surface, which is in accordance with the small intensity of the IMHP1 peak in the ion density distributions shown in Fig. 2b of the main manuscript.

6. Water distribution and orientation

Supplementary Fig. 13 displays the water density distributions across the TiO_2 interfaces with different electrolytes. Here the 1st, 2nd, 3rd, and 4th water layers are defined in accordance with Ref. [1]. We can see small differences among the water density distributions at the different interfaces, notably in the peak intensities of the 1st water layer, and the first and second sub-peaks of the 2nd water layer. These differences can be primarily attributed to the different amounts of H^+ and OH^- ions adsorbed on the TiO_2 surface for the different electrolytes.

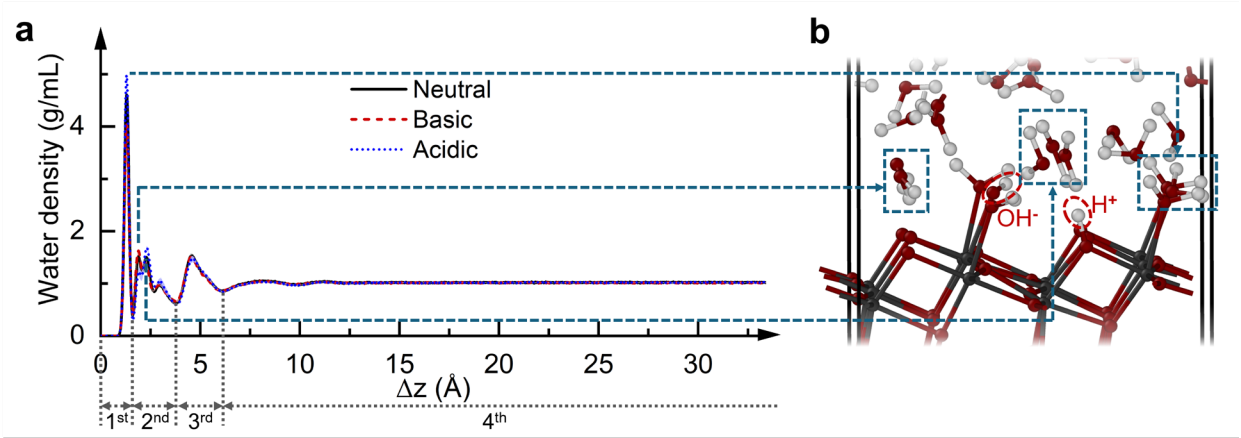

Supplementary Figure 13. a, Water density distributions as a function of distance, $\Delta z = z - z_{\text{surface}}$, from the solid surface across the TiO_2 interfaces with different electrolytes. The results are averaged over the two interfaces in the supercell, and the position of the solid surface, z_{surface}, is defined as the average location of the surface O_{2c} atoms. **b,** A representative snapshot of the

interface showing the water molecules corresponding to distinct peaks observed in the water density distribution.

As shown in Fig. 4 of the main manuscript, the TiO_2 surface's interaction with the basic, neutral and acidic electrolytes results in different coverage ratios of OH^- on the TiO_2 surface, with the order being basic ($23.3 \pm 2.7\%$) > neutral ($14.1 \pm 2.0\%$) > acidic ($9.1 \pm 2.1\%$). Conversely, the coverage ratios for H^+ are acidic ($18.3 \pm 2.1\%$) > neutral ($14.2 \pm 2.0\%$) ≈ basic ($14.2 \pm 2.0\%$). Given that the 1st water layer is comprised of adsorbed water species at Ti_{5c} sites, the occupancy of Ti_{5c} sites by OH^- reduces the quantity of intact water molecules in the 1st layer. Consequently, the intensity of the density peak for the 1st layer of water molecules in Supplementary Fig. 13a follows the sequence: basic < neutral < acidic.

The 2nd water layer comprises three sub-peaks (see Supplementary Fig. 13a). As shown in Supplementary Fig. 13b, the water in the first sub-peak (i.e., closer to the surface) generally forms two hydrogen bonds (H-bonds) with the surface O_{2c} atoms. The water molecules in the second sub-peak, situated further away from the surface, typically form one H-bond with either the surface O_{2c} atoms or an adsorbed OH^-. As shown in Supplementary Fig. 13b, when H^+ is adsorbed on O_{2c}, the 2nd layer water tends to form only one H-bond with the surface. Given the coverage order of H^+ as acidic > neutral ≈ basic, the intensity of the first sub-peak then follows the trend: acidic < neutral ≈ basic, whereas the second sub-peak's intensity follows the trend: acidic > neutral ≈ basic, as indeed shown in Supplementary Fig. 13a. Beyond the second sub-peak, the densities of water molecules in basic, neutral, and acidic systems become very similar, indicating a reduced impact of the interface on water structuring at further distances from the interface.

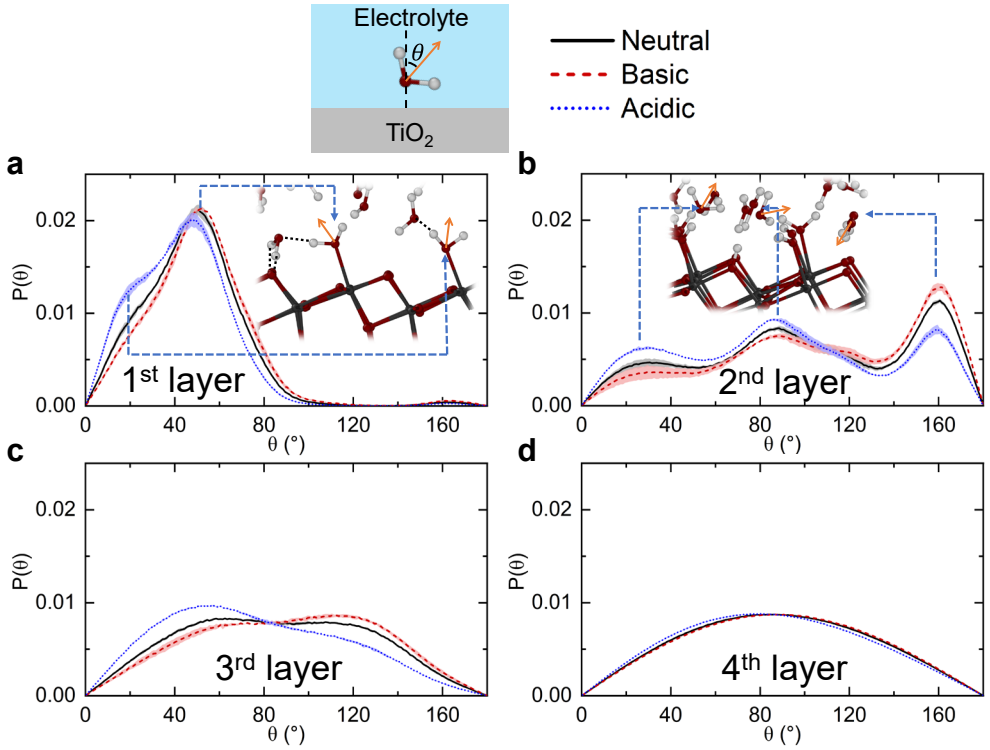

Supplementary Figure 14. Normalized probability distributions of the angle (θ) between the unit vector bisecting the two OH groups of a water molecule (indicated by orange arrows) and the surface normal for TiO_2 interfaces with various electrolytes. The 1st, 2nd, 3rd, and 4th water layers are defined in Supplementary Fig. 13a. Insets show representative atomic configurations corresponding to various peaks observed in the angular distributions. Dashed black lines show representative hydrogen bonds. For visualization purposes, only the most relevant atoms are shown.

The water angular distributions shown in Supplementary Fig. 14 reveal small differences among different electrolytes, which can also be attributed to the different amounts of H^+ and OH^- ions adsorbed on the surface. For the water molecules in the 1st water layer, the O atoms are adsorbed at Ti_{5c} sites while the hydrogen atoms form H-bonds with water molecules in the 2nd water layer, resulting in a major peak at ~50° and a shoulder at ~20° in the θ distribution as shown in Supplementary Fig. 14a. The major peak arises from water molecules in the 1st water layer that are H-bonded to the water molecules with two hydrogens pointing towards the surface[11], while the shoulder is contributed by water molecules in the 1st water layer that are H-bonded to the water molecules with only one hydrogen pointing towards the surface. When H^+ ions are adsorbed at the surface O_{2c}, the nearby water molecules in the 2nd water layer prefer to have only

one hydrogen pointing towards the surface, explaining why the shoulder is most pronounced for the interface with the acidic solution.

For the 2nd water layer, the distribution of θ features three distinct peaks centered around 30°, 90°, and 160°. The representative water molecules contributing to each peak are shown in the inset of Supplementary Fig. 14b. The peak at 30° is predominantly due to water molecules that orient both hydrogen atoms away from the surface while accepting H-bonds from the 1st layer water. The peak at 90° arises mainly from water molecules with one H atom pointing towards the surface (either donating an H-bond to surface O_{2c} or to surface OH^-) and the other pointing away from the surface. Lastly, the peak at 160° is mostly contributed by water molecules that direct both hydrogen atoms towards the surface and form two H-bonds with surface O_{2c} atoms. As already pointed out, the presence of bridging hydroxyls (i.e., O_{2c} with an adsorbed H^+) makes the water molecules orient with their H atoms away from the surface and donate fewer H-bonds to the surface, resulting in a small angle θ. Consequently, the acidic solution, which has the highest H^+ surface coverage among the three electrolytes, shows a greater probability of smaller θ angles, as shown in Supplementary Fig. 14b.

The water molecules in the 3rd water layer, being further away from the surface, are more influenced by the net surface charge than by their interaction with specific H^+ or OH^- groups adsorbed on the TiO_2 surface. This surface charge causes water molecules in a basic (acidic) electrolyte to orient their hydrogen (oxygen) atoms—towards the negatively (positively) charged surface, resulting in a larger (smaller) angle θ (see Supplementary Fig. 14c).

Regardless of the electrolyte type, the water molecules in the 4th layer exhibit a uniform distribution similar to that in bulk electrolyte solutions (Supplementary Fig. 14d). This suggests that these water molecules are almost unaffected by the surface charge because the surface charge has been well-screened by the electrical double layer.

We note that the distribution and orientation of water molecules are also influenced by the salt ions and not only by the adsorbed H^+ and OH^- ions at the surface. As elucidated in Ref. [12], water molecules in the Na^+ ion's first hydration shell preferentially orient with their oxygen ends towards Na^+, while water molecules in the Cl^- ion's first hydration shell preferentially orient the hydrogen end towards Cl^-. In this study, we did not conduct a quantitative analysis of this effect because the influence exerted by salt ions is very small relative to the impact of the surface charge. This relatively minor influence is attributed to two primary factors: first, the salt concentrations

studied in this work are low; second, within the hydration shell of a specific ion, water molecules are oriented in diverse directions, leading to a relatively uniform distribution rather than generating pronounced peaks in the probability distributions of the angle θ.

7. Electrostatic potential

To calculate the interfacial capacitance, we need the potential drop at the interface, and thus the total electrostatic potential along the surface normal z, $\phi(z)$, which is given by the sum of the contributions of the ions (nuclei + core electrons), $\phi_i(z)$, and the valence electrons, $\phi_e(z)$, namely $\phi(z) = \phi_i(z) + \phi_e(z)$. The ionic term $\phi_i(z)$is just the potential of spherical Gaussian charges with spreads given by the pseudopotential[13] to eliminate the singularities associated to point charges. While only the long-range electrostatic energy up to dipole contributions is needed for DPLR simulations, $\phi_e(z)$ depends on the actual electron density distribution. This is well approximated by the sum of Gaussian distributions centered at the WCs (obtained from the DW DNN), with spreads given by the spherical average of the spreads calculated from DFT. Unlike in the DPLR models, in this calculation, each Ti was treated as a $+12e$ ion counterbalanced by a $-8e$ charge from its WCs. The potential $\phi_e(z)$ was then calculated by Fourier transform of the following reciprocal space expression:

$$\phi_e(m_z) = \frac{-1}{\pi {m_z}^2} \sum_{i=1}^{n_{\mathrm{WC}}} q_{\mathrm{WC}}^i \, exp\left(-i2\pi m_z z_{\mathrm{WC}}^i\right) \exp\left(-\frac{\pi^2 m_z^2}{2{\beta_z^i}^2}\right), \tag{5}$$

Here $m_z = \frac{K_z}{2\pi}$ where K_z is a reciprocal lattice vector in the z direction, n_{WC} is the total number of WCs, z_{WC}^i is the z-coordinate of the ith WC, $(2\beta_z^i)^{-1}$ the corresponding z-spread, and q_{WC}^i (= –8e) is the charge of the ith WC. The negative sign before the summation indicates that $\phi_e(z)$ is the electrostatic potential experienced by electrons. Note that the term K_z =0 in Eq. (4) is cancelled by the analogous term from $\phi_i(z)$.

To validate our procedure, we compared the electrostatic potential calculated using our methodology with the potential given by DFT, both averaged over 50 configurations extracted from DPLR MD simulations of a (1 × 3) anatase (101) slab interface slab in contact with a 20 Å thick layer of aqueous NaCl solution (see Supplementary Fig. 15a). As illustrated in

Supplementary Fig. 15b, our computed $\phi(z)$ closely reproduces the DFT result, confirming the accuracy and reliability of our approach.

Our approach to retrieve the electrostatic potential can be used to calculate the difference between the average electrostatic potentials in the solid and the solution, which is the quantity of interest in our study. However, it is well known that computing absolute potentials requires the use of appropriate strategies when using periodic boundary conditions. This issue has been discussed extensively in the literature[14]. The integration of such strategies with our approach is an interesting topic to explore in future studies.

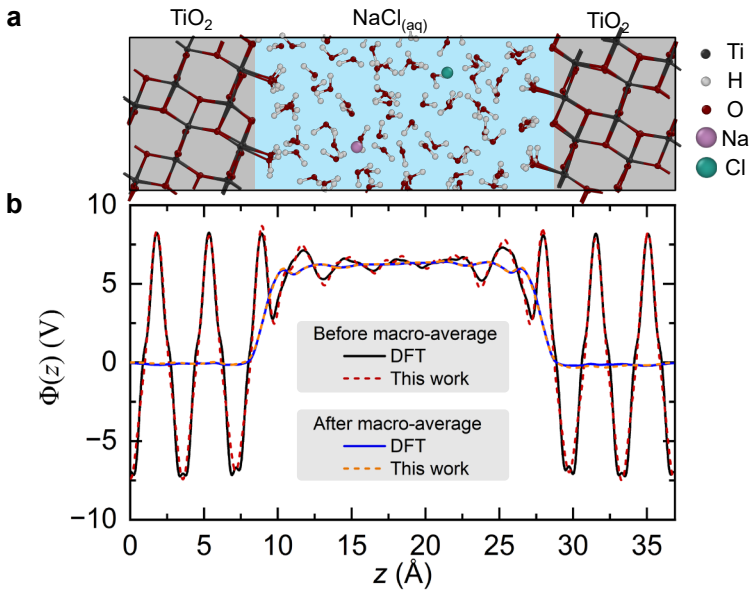

Supplementary Figure 15. a, Representative snapshot of the anatase (101)-NaCl solution interface used to validate our procedure for calculating the electrostatic potential. **b,** Plane-averaged electrostatic potential, $\phi(z)$, along the z-direction of the interface, before and after macro-average[15]. Results obtained using DFT and our developed methodology are presented in solid and dashed lines, respectively.

8. Finite cell size limitation and comparison to experiment

Although the size of our simulation box is quite large by AIMD standards, it is not large enough to allow establishment of equilibrium in the exchanges of water ions between the surface and the bulk reservoir. This limitation prevents us from reproducing the relationship between pH

and surface charge density, σ, that is observed in experiments. Specifically, in our simulations all H^+ and OH^- ions in the acidic and basic electrolyte were adsorbed on the TiO_2 surface, leading to $\sigma_a \approx 7.7\ \mu C/cm^2$ and $\sigma_b \approx -7.5\,\mu C/cm^2$, respectively, with no water ions in the bulk region of the electrolyte. In the experiment, on the other hand, such values of σ_a and σ_b are observed at solution pHs of $\approx$ 4.4 and 7.4[9], respectively, two pH values that are not accessible to our simulations. However, the above limitation does not affect our results for the structure and capacitance of the EDL because a pH value of 4.4 (or 7.4) corresponds to a negligible amount of $\sim 2 \times 10^{-3}$ H^+ (or 1×10^{-5} OH^-) ions in our electrolyte solution.

Another limitation of the finite cell size is the difference in ion concentration between neutral and acidic or basic systems. To change the pH of the systems, we added 0.2 M HCl or 0.2 M NaOH to 0.4 M NaCl solution. This procedure follows the titration experiment protocol[16,17]. In the experimental setup, the ionic strength remains essentially unchanged due to the large size of the system. Instead, the addition of NaOH and HCl to our finite-sized simulation cell alters the ionic strength. After equilibration with the electrical double layer, the average Na^+ and Cl^- concentrations in the bulk electrolyte region for the neutral, basic, and acidic systems are 0.34 ± 0.02, 0.41 ± 0.02, and 0.45 ± 0.08 M, respectively. The differences in ionic concentration among these three systems are relatively small, with the neutral system showing a somewhat lower ion concentration compared to the basic and acidic systems. To assess the impact of this difference in ionic concentration, we conducted an additional DPLR molecular dynamics simulation of the TiO_2 interface with a neutral NaCl electrolyte at a higher initial salt concentration of 0.5 M. After equilibration, the ionic density distribution of this TiO_2-0.5 M $NaCl_{(aq)}$ system (Supplementary Fig. 16) is very similar to that of the TiO_2-0.4 M $NaCl_{(aq)}$ system in Fig. 2b of the main manuscript in the region close to the interface. However, the average Na^+ and Cl^- concentration of the 0.5 M $NaCl_{(aq)}$ solution in the bulk electrolyte region was found to be 0.44 ± 0.10 M, which is closer to the ion concentrations of the basic and acidic solutions compared to the original 0.4 M $NaCl_{(aq)}$ system. Using the 0.5 M $NaCl_{(aq)}$ system as a reference, we obtained capacitance values under acidic and basic conditions of $C_a = 63.4 \pm 2.6\,\mu F/cm^2$ and $C_b = 87.9 \pm 5.7\,\mu F/cm^2$, respectively, yielding a ratio of $C_b/C_a = 1.4 \pm 0.1$, which is comparable to the value of $C_b/C_a = 1.6 \pm 0.3$ obtained using the 0.4 M $NaCl_{(aq)}$ reference, and aligns well with the experimental estimate of $C_b/C_a \approx 1.5$. This indicates that the small differences in ionic strength among neutral, basic and acidic solutions do not affect the conclusions of our study.

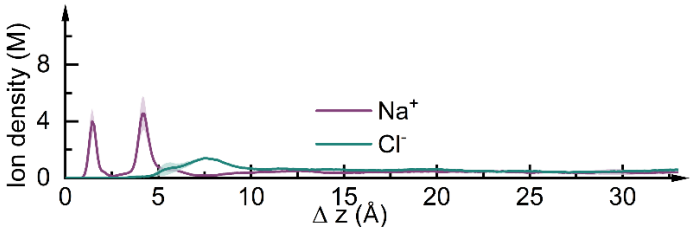

Supplementary Figure 16. Ion density distributions as functions of distance $\Delta z = z - z_{\text{surface}}$ from the solid surface, obtained from DPLR simulations of anatase (101) in contact with 0.5 M $NaCl_{(aq)}$. The position of the solid surface, z_{surface}, corresponds to the average position of the surface O_{2c} sites. The simulation were conducted for 5 ns at 330 K with the first 3 ns discarded for equilibration purposes. The error bars were derived from simulations using two independent DPLR models.

9. Na^+ ions adsorbed at O_{2c}

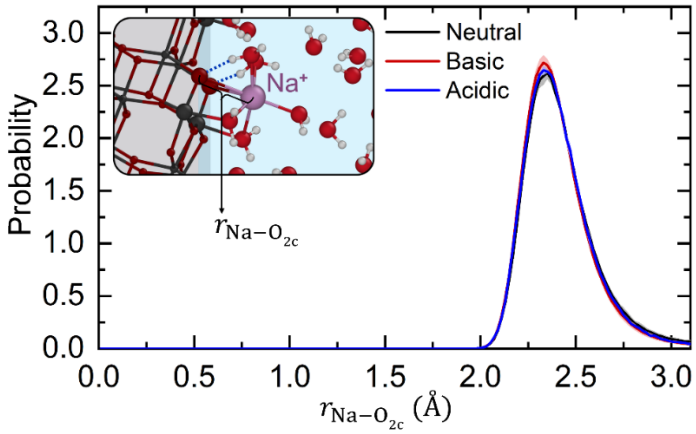

Supplementary Figure 17. Normalized probability distribution of the distance between the Na^+ in the IHP and O_{2C} atoms at the TiO_2 surface, which is denoted as $r_{\text{Na-O2c}}$. The inset schematically shows the definition of $r_{\text{Na-O2c}}$.

10. TiO_2 interface with concentrated (0.4 M) NaOH and HCl solutions

To further validate our conclusions, we conducted DPLR MD simulations of TiO_2 interfaces for higher surface charge densities compared to those presented in the main manuscript. Specifically, we simulated the TiO_2 interface with acidic (0.4 M NaCl + 0.4 M HCl) and basic (0.4

M NaCl + 0.4 M NaOH) solutions using the simulation conditions and cell size used for the simulations reported in the main text. The increased HCl and NaOH concentrations resulted in larger surface charge densities of $\sigma_{a'} = 12.99 \pm 0.21\ \mu C/cm^2$ and $\sigma_{b'} = -13.62 \pm 0.14\ \mu C/cm^2$ for the acidic and basic systems, respectively.

The ion density distributions of these two higher concentration systems (Supplementary Figure 18) exhibit the same features as the system presented in Fig. 2b of the main manuscript, but with large differences between the neutral, basic, and acidic systems due to the increased surface charge densities. Specifically, in the higher concentration basic system, more Na^+ ions are drawn close to the surface to screen the higher negative surface charge density, resulting in a first Na^+ peak with intensity as high as 25 M. This leads to a large capacitance of $C_{b'} = 130.9 \pm 14.4\ \mu F/cm^2$. In contrast, for the higher concentration acidic system, there is only a modest increase in the Cl^- peak intensity due to the repulsion between the negatively charged Cl^- ion and the electronegative O_{2c} atoms. Consequently, the capacitance of the higher concentration acidic system increases only slightly, viz. $C_{a'} = 63.1 \pm 2.8\ \mu F/cm^2$. These calculated capacitances agree well with the experimental results as shown in Fig. 3c of the main manuscript.

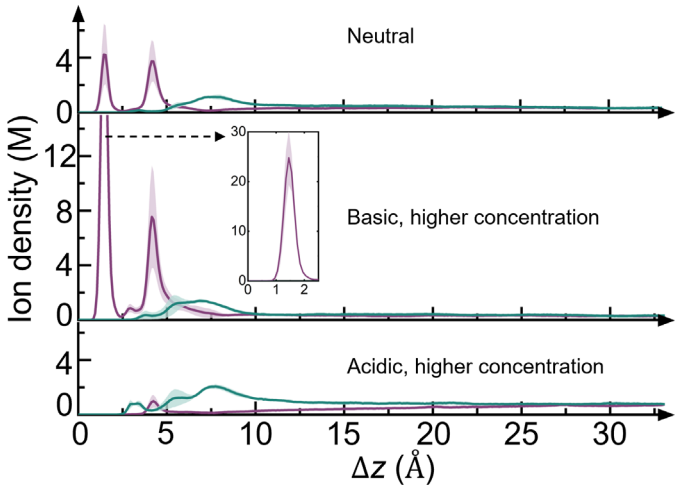

Supplementary Figure 18. Ion density distributions as functions of distance, Δz, from the solid surface, obtained from DPLR simulations of anatase (101) in contact with higher concentration acidic (0.4 M NaCl + 0.4 M HCl) and basic (0.4 M NaCl + 0.4 M NaOH) solutions, compared to that of the neural 0.4 M NaCl solution.

References

1 Calegari Andrade, M. F., Ko, H.-Y., Car, R. & Selloni, A. Structure, Polarization, and Sum Frequency Generation Spectrum of Interfacial Water on Anatase TiO_2. *The Journal of Physical Chemistry Letters* **9**, 6716-6721 (2018). https://doi.org/10.1021/acs.jpclett.8b03103

2 Calegari Andrade, M. F., Ko, H.-Y., Zhang, L., Car, R. & Selloni, A. Free energy of proton transfer at the water–TiO_2 interface from ab initio deep potential molecular dynamics. *Chemical Science* (2020). https://doi.org/10.1039/c9sc05116c

3 Thompson, A. P. *et al.* LAMMPS - a flexible simulation tool for particle-based materials modeling at the atomic, meso, and continuum scales. *Computer Physics Communications* **271** (2022). https://doi.org/10.1016/j.cpc.2021.108171

4 Wang, H., Zhang, L., Han, J. & E, W. DeePMD-kit: A deep learning package for many-body potential energy representation and molecular dynamics. *Computer Physics Communications* **228**, 178-184 (2018). https://doi.org/10.1016/j.cpc.2018.03.016

5 Tribello, G. A., Bonomi, M., Branduardi, D., Camilloni, C. & Bussi, G. PLUMED 2: New feathers for an old bird. *Computer Physics Communications* **185**, 604-613 (2014). https://doi.org/10.1016/j.cpc.2013.09.018

6 Grifoni, E., Piccini, G. & Parrinello, M. Microscopic description of acid–base equilibrium. *Proceedings of the National Academy of Sciences* **116**, 4054-4057 (2019). https://doi.org/10.1073/pnas.1819771116

7 Raman, A. S. & Selloni, A. Acid-Base Chemistry of a Model IrO(2) Catalytic Interface. *J Phys Chem Lett* **14**, 7787-7794 (2023). https://doi.org/10.1021/acs.jpclett.3c02001

8 Bourikas, K., Vakros, J., Kordulis, C. & Lycourghiotis, A. Potentiometric Mass Titrations: Experimental and Theoretical Establishment of a New Technique for Determining the Point of Zero Charge (PZC) of Metal (Hydr)Oxides. *The Journal of Physical Chemistry B* **107**, 9441-9451 (2003). https://doi.org/10.1021/jp035123v

9 Ridley, M. K., Machesky, M. L. & Kubicki, J. D. Anatase Nanoparticle Surface Reactivity in NaCl Media: A CD–MUSIC Model Interpretation of Combined Experimental and Density Functional Theory Studies. *Langmuir* **29**, 8572-8583 (2013). https://doi.org/10.1021/la4011955

10 Kosmulski, M. Isoelectric points and points of zero charge of metal (hydr)oxides: 50years after Parks' review. *Advances in Colloid and Interface Science* **238**, 1-61 (2016). https://doi.org/https://doi.org/10.1016/j.cis.2016.10.005

11 Mattioli, G., Filippone, F., Caminiti, R. & Amore Bonapasta, A. Short Hydrogen Bonds at the Water/TiO_2 (Anatase) Interface. *The Journal of Physical Chemistry C* **112**, 13579-13586 (2008). https://doi.org/10.1021/jp8031176

12 Zhang, C., Yue, S., Panagiotopoulos, A. Z., Klein, M. L. & Wu, X. Why Dissolving Salt in Water Decreases Its Dielectric Permittivity. *Physical Review Letters* **131**, 076801 (2023). https://doi.org/10.1103/PhysRevLett.131.076801

13 Hamann, D. R. Optimized norm-conserving Vanderbilt pseudopotentials. *Physical Review B* **88**, 085117 (2013). https://doi.org/10.1103/PhysRevB.88.085117

14 Le, J., Iannuzzi, M., Cuesta, A. & Cheng, J. Determining Potentials of Zero Charge of Metal Electrodes versus the Standard Hydrogen Electrode from Density-Functional-Theory-Based Molecular Dynamics. *Phys Rev Lett* **119**, 016801 (2017). https://doi.org/10.1103/PhysRevLett.119.016801

15 Baldereschi, A., Baroni, S. & Resta, R. Band Offsets in Lattice-Matched Heterojunctions: A Model and First-Principles Calculations for GaAs/AlAs. *Physical Review Letters* **61**, 734-737 (1988). https://doi.org/10.1103/PhysRevLett.61.734

16 Bérubé, Y. G. & de Bruyn, P. L. Adsorption at the rutile-solution interface: I. Thermodynamic and Experimental Study. *Journal of Colloid and Interface Science* **27**, 305-318 (1968). https://doi.org/10.1016/0021-9797(68)90038-6

17 Bérubé, Y. G. & de Bruyn, P. L. Adsorption at the rutile-solution interface: II. Model of the electrochemical double layer. *Journal of Colloid and Interface Science* **28**, 92-105 (1968). https://doi.org/10.1016/0021-9797(68)90211-7